Journal of Molecular Structure 1369 (2026) 146331

Contents lists available at ScienceDirect

Journal of Molecular Structure

journal homepage: www.elsevier.com/locate/molstr

Synthesis, growth, structural and comprehensive analysis of a potential single crystal for third-order NLO applications: Experimental and theoretical insights

P Hemalatha [a], M Mohanraj [a], S Anandhi [b], H Jemmy Chirsty [c], T C Sabari Girisun [d], M Parthasarathy [a,*]

[a] Department of Physics, School of Basic Sciences, Vels Institute of Science, Technology and Advanced Studies, Pallavaram, Chennai 600 117, Tamilnadu, India
[b] Department of Physics, Sathyabama Institute of Science and Technology, Chennai, Tamil Nadu 600119, India
[c] Department of Bioinformatics, Sathyabama Institute of Science and Technology, Chennai, Tamil Nadu 600119, India
[d] Nanophotonics Laboratory, School of Physics, Bharathidasan University. Tiruchirappalli 620 024, Tamil Nadu, India

ARTICLE INFO

Keywords:
Structural refinement
Frontier molecular orbital (FMO)
Hirshfeld surface analysis
Hyperpolarizability
Reverse saturable absorption (RSA)

ABSTRACT

Semi-organic nonlinear optical single crystals are vital to current photonic technologies because they combine the organic flexibility and inorganic stability. The third-order semi-organic NLO single crystal, D-Phenylglycinium bromide (DPGBr), was successfully synthesised by slow evaporation from an aqueous solution. The structural refinement of the crystal was elucidated with the SHELX-97, which concluded that it crystallises in the orthorhombic system with space group $P2_12_12_1$. Extensive structural, spectroscopic, optical, thermal, and theoretical analyses were conducted. The molecular geometry has been optimised and is consistent with the experimental data, validating the theoretical model. FT-IR and FT-Raman spectra are consistent with computational vibrational frequencies, allowing functional group assignments. Optical properties were evaluated using UV–visible-NIR and photoluminescence spectroscopy. The energy difference between HOMO and LUMO is 4.415 eV, indicating high stability in kinetic properties and charge transfer. The molecular electrostatic potential map shows that intermolecular interactions influence both bromide and heteroatom sites, which exhibit large negative potentials. The Hirshfeld surface analysis reveals that Van der Waals forces and hydrogen bonding affect molecular packing. The material's hyperpolarizability (α_0) demonstrates a strong NLO response. EDAX verified the elemental composition, and thermal stability (TG-DTA/DSC) testing showed it is stable up to 235 °C. Measurements of reverse saturable absorption with a nonlinear absorption coefficient of 0.48×10^{-10} m/W and an optical limiting threshold of 6.24×10^{12} W/m^2 indicated that it is a promising material for photonic and optical limiting applications.

1. Introduction

In recent years, organic crystalline salts have been of considerable interest as promising materials for third-order nonlinear optical applications. Their high molecular polarity, extensive π-electron conjugation, and ability to facilitate efficient intramolecular charge transfer make them the best candidates for the development of sophisticated photonic and optoelectronic devices. Developing new organic materials with enhanced optical properties is increasingly important for advancing photonic and optoelectronic technologies. These materials have been successfully applied to terahertz (THz) wave generation and measurement, holographic imaging, optical limiting, high-speed data processing, integrated photonics, optical communication, laser monitoring, optical computing, and frequency conversion [1–4]. The organic molecules may serve as electron donors and acceptors due to their inherent polarity, chirality, and extended, electron-conjugated structures. There is great interest in organic nonlinear optical materials due to their large electro-optic coefficients, low dielectric constants, fast response times, and large nonlinear optical responses [5–7]. Incorporating aromatic rings into organic compounds confers them with peculiar properties, including a high laser-damage threshold, a robust nonlinear optical response, high molecular polarity, and reduced

* Corresponding author.
E-mail address: mps2k7@gmail.com (M. Parthasarathy).

https://doi.org/10.1016/j.molstruc.2026.146331
Received 11 February 2026; Received in revised form 9 April 2026; Accepted 19 April 2026
Available online 20 April 2026

charge-carrier mobility. These characteristics make organic NLO materials a good choice for next-generation photonic devices compared to inorganic systems. Improvement in NLO performance is primarily achieved by incorporating donor-π-acceptor structures, which facilitate efficient electron transfer [8–10]. Extended π-conjugation enables optimal electronic interaction between donor and acceptor groups, leading to greater charge delocalisation and optical nonlinearity [11–13]. Moreover, these π-conjugated systems are mechanically, photochemically, and thermally stable, which is key to generating stable and efficient third-order NLO devices [14,15]. Phenylglycine is an essential raw material in the production of β-lactam antibiotics, such as semisynthetic penicillins and cephalosporins [16,17]. Its halogenated analogues are found to be genotoxic amino acids [18,19]. Its structure contains an aromatic ring, enabling non-covalent interactions, including π-π stacking, which are widespread in biological systems and are a central component of medicinal chemistry [20]. D-Phenylglycine hydrochloride [21], D-Phenylglycinium nitrate [22], D-Phenylglycine perchlorate [23], Bis-Glycine hydrochloride [24], and Bis (D-Phenylglycinium) sulphate monohydrate [25] have been reported to adopt crystal forms. In addition to the extensive studies reported in the literature, our research team thoroughly characterised the crystal structure of the synthesised product, which is deposited in the CCDC number: 935,608 [26]. We conducted an extensive theoretical and experimental study, the first of its kind, and now we can make meaningful comparisons and understand its peculiarities. This paper is a close examination of the synthesis and detailed characterisation of a D-Phenylglycinium bromide (DPGBr) single crystal using the SEST method at room temperature. Thorough research was conducted using X-ray diffraction, Hirshfeld surface analysis, and molecular geometry assessment. The Kurtz-Perry powder test and third-order NLO measurements were carried out, whereas the vibrational modes were analysed using FT-IR and FT-Raman spectroscopic analysis. Additionally, the frontier molecular orbitals (FMOs) and hyperpolarizability were calculated using the TD-DFT method. The optical characteristics, including UV absorbance and photoluminescence, were evaluated. TG-DTA/DSC and EDAX studies assess the thermal stability and its elemental composition. The close agreement between the experimental results and the theoretical calculations demonstrates the validity of the data and provides useful insights into the compound's molecular structure, vibrational features, optical properties, and thermal stability.

2. Experimental procedure

D-Phenylglycine and hydrobromic acid were purchased from Sigma-Aldrich with a purity of 99% and mixed in an equimolar (1:1) ratio in water as the solvent. The solution was stirred for 6 hrs to obtain a homogeneous, saturated solution. The solution was filtered through Whatman filter paper, which removed any remaining impurities that could compromise the final product's integrity. To ensure the solution remained stable throughout crystallisation, the filtered solution was placed in a well-controlled environment free of thermal variations and mechanical interference. Good-quality, transparent optical single crystals of DPGBr were harvested after 45 days, as shown in Fig. 1., and the reaction mechanism is depicted in Scheme 1.

Solubility studies were systematically carried out across a temperature range of 30° to 50 °C. For each measurement, a specific amount of salt was dissolved in deionised water, with the temperature maintained constant. Continuous stirring was applied to ensure uniformity and promote effective dissolution. After reaching saturation, the solute's equilibrium concentration was determined gravimetrically [27]. The results showed a positive temperature gradient along the solubility curve, indicating that the solubility of the DPGBr salt in water increases with temperature (Fig. 2).

3. Results and discussion

3.1. X-ray diffraction analysis

The X-ray diffractometer analysed the DPGBr in single-crystal mode (Bruker AXS Kappa Apex II) using MoKα (λ = 0.71073 Å) radiation. The structure was well refined by full-matrix least-squares using the SHELX-97 program [28], and it was confirmed to crystallise in the orthorhombic space group $P2_12_12_1$. The parameters of the unit cell are a = 5.5240(5) Å, b = 7.4735(5) Å, and c = 23.1229(18) Å, with a unit cell volume of 954.60(13) Å^3. Tables 1 and 2 present the crystallographic and structural refinements, including the hydrogen-bonding geometry of DPGBr. Optimization automatically achieved R = 0.022, w$R(F^2)$ = 0.046, and a goodness-of-fit (S) = 1.03 with 2170 reflections. The Flack value of 0.011(8) supports the assignment of the absolute configuration as the Denantiomer. The final Fourier map showed minor residual electron density (Δρ = 0.25 eÅ^{-3}), indicating a reliable refinement with no significant errors. The asymmetric unit (Fig. 3.) has a distinct non-planar geometry of the D-Phenylglycinium cation, with the carboxyl group slightly out of the plane of the phenyl ring. The torsion angle N1-C7-C8-O1 = 15.6(3)° suggests a slight non-coplanarity between the amino and carboxyl groups, likely due to low conjugation. The C = O and C–O bond lengths are 1.192(3) Å and 1.323(3) Å, respectively, corresponding to localised double and single bonds. The N—C bond length of 1.497(2) Å indicates partial delocalisation of the electrons between nitrogen and the carboxylic group via resonance. The α-carbon (C7) is nearly tetrahedral, with angles between 107° and 112°, confirming sp^3 hybridisation. These geometric parameters align well with those of previously reported related amino acid halides, such as D-Phenylglycinium chloride, suggesting no significant distortion in the molecular conformation due to halide substitution [29].

The structural framework is primarily stabilised by an intermolecular hydrogen-bond network. The protonated amino nitrogen is donating in a number of NH- H-bromide anion interactions, and the carboxylic OH group is contributing an additional OH-bromide interaction. The strongest directional forces in the lattice are N—H…Br, with D… A distance of interactions from 3.3166(18) to 3.429(2) Å, and the angles are 154° to 164°. The O—H…Br interaction (3.2027(17)Å, 171°)

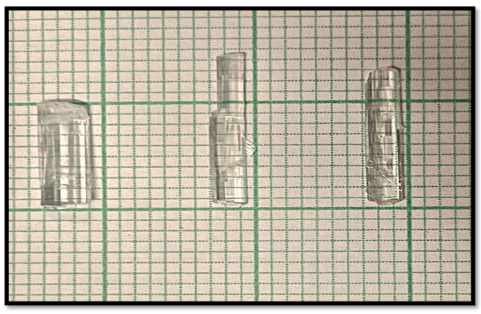

Fig. 1. As-grown single crystals of D-Phenylglycinium bromide.

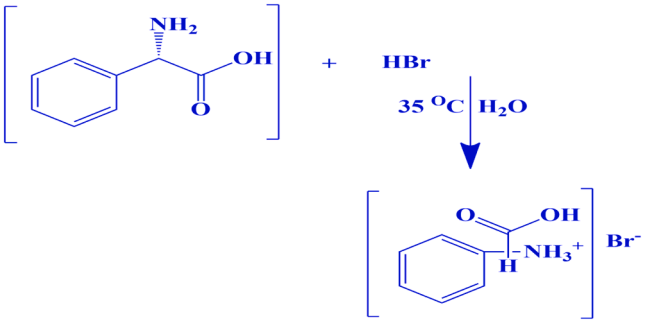

Scheme 1. Reaction Mechanism of DPGBr.

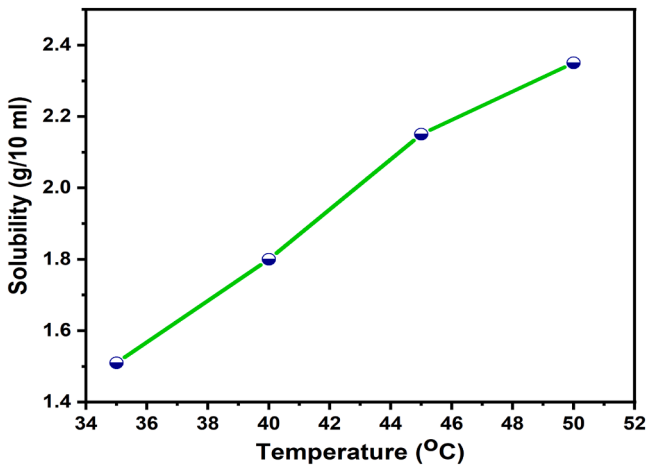

Fig. 2. Solubility curve of DPGBr.

Table 1
Crystal data and structure refinement data of DPGBr.

Empirical formula	$C_8H_{10}NO_2^+.Br^-$
Formula weight	232.08
Temperature	295K
Wavelength	0.71073 Å
Crystal system	Orthorhombic
Space group	$P2_12_12_1$
Unit cell dimensions	a = 5.5240(5) Å b = 7.4735(5) Å c = 23.1229 (18)Å
Volume	V = 954.60(13) $Å^3$
Z	4
Density (calculated)	1.615 Mg/m^3
Index ranges	$-6 \le h \le 7$, $-9 \le k \le 5$, $-28 \le l \le 30$
Reflections collected	5824
Independent reflections	2170[R(int) = 0.022]
Data/restraints/parameters	2170/ 0 / 114
Goodness-of-fit on F2	1.03
Final R indices [I > 2sigma(I)]	R1 = 0.022, wR2 = 0.046

Table 2
Hydrogen bonding geometry (Å°) of DPGBr.

D–H…A	D–H	H…A	D…A	D–H…A
N1–H1B…Br1^{i}	0.89	2.54	3.3586(17)	154
N1–H1C…Br1^{ii}	0.89	2.57	3.429(2)	163
N1–H1A…Br1	0.89	2.45	3.3166(18)	164
O1–H1D…Br1^{iii}	0.82	2.39	3.2027(17)	171
C7–H7…O2^{iv}	0.98	2.59	3.527(3)	159

Symmetry codes: (i) $-x+1, y-1/2, -z+3/2$; (ii) $x-1, y, z$; (iii) $x-1, y-1, z$; (iv) $x+1, y, z$.

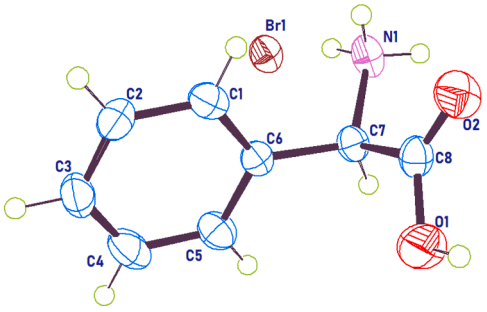

Fig. 3. ORTEP diagram of DPGBr.

further indicates the ionic connectivity and weak C—H…O interaction (3.527(3) Å, 159°) provides further stabilisation. These hydrogen bonds form a large, three-dimensional network that defines the overall arrangement of the molecules. The packing diagram (Fig. 4.) indicates that bromide ions play a crucial role in the organisation of the molecular structure by connecting the neighbouring D-phenylglycinium cations into two-dimensional hydrogen-bonded sheets that are perpendicular to the (001) plane. Weaker van der Waals forces along the c-axis further bind these sheets, forming a compact, highly ordered three-dimensional supramolecular network.

The powder X-ray diffraction results were obtained using a Bruker D2 Phaser spectrometer with Cu Kα radiation (λ = 1.5418 Å) at a scanning rate of 1 °/min. The sharp peaks in the diffraction patterns were systematically indexed using the POWDER X refinement software package, enabling detailed analysis of the material's crystalline structure. Fig. 5. provides a comprehensive comparison of the indexed powder X-ray diffraction patterns of DPGBr with the corresponding theoretical data. Notably, the absence of unindexed reflection ratios, along with the lack of additional peaks, strongly suggests that the synthesised material is free from secondary phases or domains that could affect its integrity. Furthermore, a thorough comparison of the main peaks in the experimental and theoretical results was performed, enhancing the correlation between the two data sets. This careful alignment not only confirms the sample's purity but also supports the reliability of the characterisation methods used throughout this study.

The specific elements present in the material were identified from the distinctive peaks observed in the EDAX spectrum shown in Fig. 6. These findings strongly indicate that the material is not only free of impurities but also synthesised with high purity. Moreover, the EDAX results further reinforce the conclusion that this material is highly pure, making it well-suited for applications in cutting-edge technology and photonics.

3.2. *Molecular geometry analysis*

The results of Density Functional Theory (DFT) calculations for optimized molecular geometry parameters, performed using the LANL2DZ/6–311++G(d,p) basis set, were compared with those obtained from X-ray diffraction analysis. Table 3 displays the molecular geometry of DPGBr. The optimised geometry of DPGBr is shown in Fig. 7. Bond length and angle analyses of DPGBr show good agreement between experimental (XRD) and theoretical (DFT) results, confirming the reliability of the optimised structure [30,31]. The C–C bond lengths in the aromatic ring range from 1.361 to 1.389 Å (XRD) and 1.392 to 1.399 Å (DFT), indicating typical aromatic character with π-electron delocalisation. The C6–C7 and C7–N1 bond lengths are consistent with strong σ-bonding interactions, while the C8–O2 and C8–O1 bond lengths confirm the presence of localised double and single bonds in the carboxyl group with partial electron delocalisation. The bond angles within the phenyl ring (~119°–121°) confirm sp^2 hybridisation,

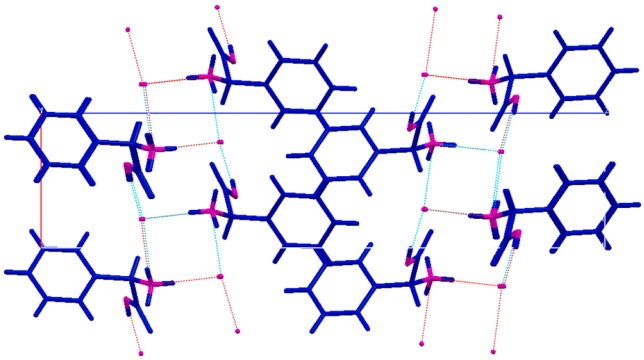

Fig. 4. Hydrogen Bonding interaction of DPGBr.

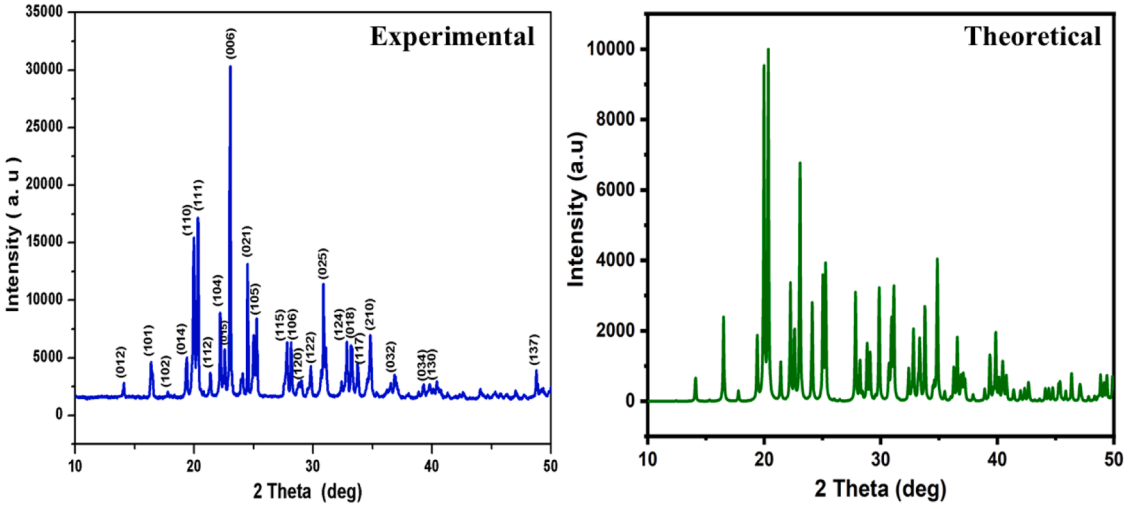

Fig. 5. Experimental and Theoretical PXRD pattern of DPGBr.

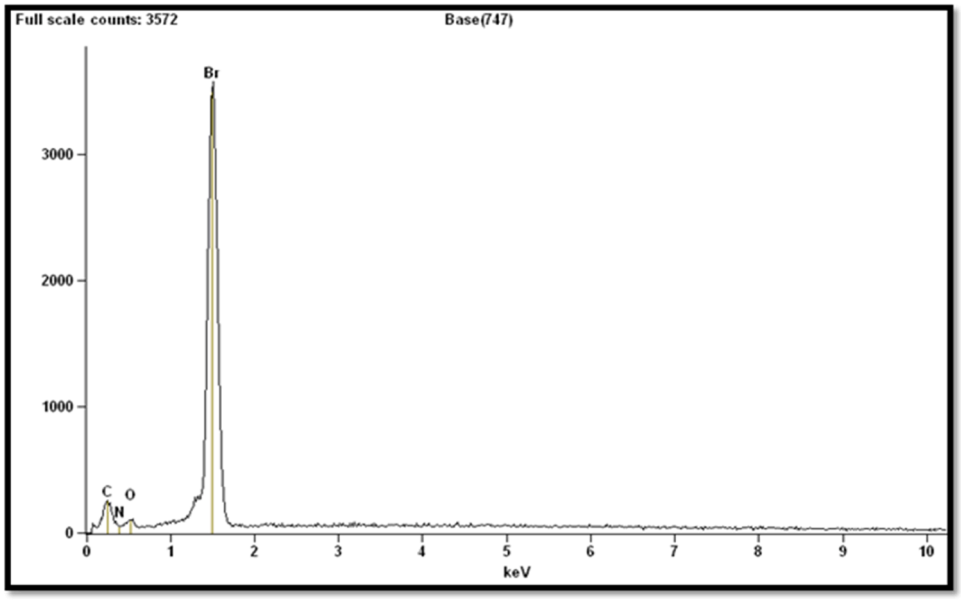

Fig. 6. EDAX spectrum of DPGBr.

whereas the bond angles around the α-carbon (C7) (107°–112°) indicate a slightly distorted tetrahedral geometry due to intermolecular interactions. The conformational analysis of the title molecule reveals that it adopts a twisted non-planar conformation, as supported by both experimental (XRD) and theoretical (DFT) results. The phenyl ring is essentially planar, as confirmed by the near-zero torsional angles (C6–C1–C2–C3 = 0.2° and C1–C2–C3–C4 = −0.3°), indicating strong π-conjugation within the aromatic system. However, significant deviations are observed in the torsional angles involving the C6–C7–C8 linkage, such as C1–C6–C7–N1 (−54.0°) and C1–C6–C7–C8 (66.2°), demonstrating that the side chain is twisted relative to the phenyl ring. Furthermore, the torsional angles N1–C7–C8–O2 (15.6°) and N1–C7–C8–O1 (−165.48°) indicate that the carboxyl group is not perfectly coplanar with the molecular backbone. These features confirm that the molecule adopts a non-planar, twisted conformation, which is attributed to reduced conjugation and intermolecular hydrogen bonding in the crystal lattice. Such a conformation is typical for amino acid derivatives and plays a significant role in molecular packing and optical properties.

3.3. *Vibrational spectral analysis*

Experimental FT-IR and FT-Raman spectroscopy were employed to investigate the vibrational characteristics of DPGBr, and the results were correlated with frequencies calculated at the LANL2DZ/6–311++G(d,p) level of theory. A scaling factor of 0.967 was applied to the computed frequencies to account for anharmonicity and the systematic overestimation inherent in DFT calculations [32,33]. The excellent agreement between experimental FT-IR and FT-Raman wavenumbers and the calculated wavenumbers, supported by potential energy distribution (PED) analysis, confirms the reliability of the optimised molecular structure. The detailed assignments along with PED contributions are presented in Table 4. The experimental and calculated (theoretical) FT-IR and FT-Raman spectra of DPGBr are shown in Fig. 8a and 8b, respectively.

O–H and N–H Stretching Vibrations

The FT-IR band at 3607 cm^{-1} and the corresponding Raman band at 3600 cm^{-1} are assigned to the ν(O–H) stretching vibration, with a dominant PED contribution of 99%, confirming its pure hydroxyl

Table 3
Molecular Geometry of DPGBr.

Bond length	XRD (Å)	DFT(Å)	Bond length	XRD(Å)	DFT(Å)
C1—C6	1.382 (3)	1.399	C6—C7	1.515 (2)	1.52
C1—C2	1.383 (3)	1.395	C7—N1	1.497 (2)	1.507
C2—C3	1.361 (3)	1.393	C7—C8	1.507 (3)	1.514
C3—C4	1.365 (3)	1.396	C8—O2	1.192 (3)	1.217
C4—C5	1.389 (3)	1.392	C8—O1	1.323 (3)	1.336
C5—C6	1.386 (3)	1.399			
Bond Angle	**XRD (°)**	**DFT(°)**	**Bond Angle**	**XRD(°)**	**DFT(°)**
C6—C1—C2	119.8 (2)	119.8	C5—C6—C7	119.15 (19)	118.9
C3—C2—C1	120.6 (2)	120.2	N1—C7—C8	107.37 (17)	107.8
C2—C3—C4	120.4 (2)	119.9	N1—C7—C6	112.12 (15)	110.8
C3—C4—C5	120.0 (2)	119.9	C8—C7—C6	111.19 (16)	113.1
C6—C5—C4	119.9 (2)	120.18	O2—C8—O1	125.1 (2)	123.89
C1—C6—C5	119.30 (19)	119.8	O2—C8—C7	124.73 (19)	123.8
C1—C6—C7	121.4 (2)	121.2	O1—C8—C7	110.16 (19)	111.3
Torsional Angle	**XRD(°)**	**DFT(°)**	**Torsional Angle**	**XRD(°)**	**DFT(°)**
C6—C1—C2—C3	0.2 (4)	0.15	C1—C6—C7—N1	−54.0 (3)	93.73
C1—C2—C3—C4	−0.3 (4)	0.06	C5—C6—C7—N1	130.1 (2)	−84.06
C2—C3—C4—C5	0.5 (4)	−0.13	C1—C6—C7—C8	66.2 (2)	−144.16
C3—C4—C5—C6	−0.6 (3)	−0.03	C5—C6—C7—C8	−109.7 (2)	38.03
C2—C1—C6—C5	−0.2 (3)	−0.32	N1—C7—C8—O2	15.6 (3)	5.49
C2—C1—C6—C7	−176.2 (2)	−178.1	C6—C7—C8—O2	−107.4 (2)	−118.22
C4—C5—C6—C1	0.5 (3)	0.25	N1—C7—C8—O1	−165.48 (17)	172.97
C4—C5—C6—C7	176.5 (2)	178.04	C6—C7—C8—O1	71.5 (2)	63.3

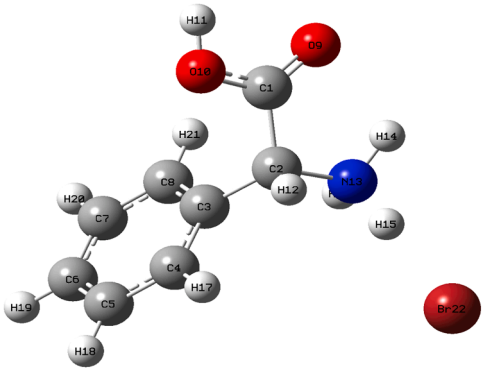

Fig. 7. Optimized Geometry of DPGBr.

character. The bands observed at 3386 cm^{-1} (FTIR) and 3350 cm^{-1} (Raman) correspond to ν(N–H) stretching modes, with PED contributions of 94–96%. The shift of these bands to lower wavenumbers relative to free stretching vibrations indicates strong intermolecular hydrogen bonding, consistent across both spectra.

C–H Stretching Vibrations

The aromatic ν(C–H) stretching vibrations appear at 3079 cm^{-1} and 3060 cm^{-1} (FTIR) and at 3050 cm^{-1} (Raman), with PED contributions of 85–92%, confirming dominant ring hydrogen motion. The aliphatic ν(C–H) stretching modes are observed at 2992 cm^{-1} (FTIR) and 2990 cm^{-1} (Raman), in good agreement with the calculated values. A weak band at 2695 cm^{-1} (FTIR) and 2690 cm^{-1} (Raman) arises due to overtone or combination bands, with mixed PED contributions (<50%), indicating coupled vibrational behaviour [34–36].

Carbonyl and Imine Vibrations

A strong absorption band at 1725 cm^{-1} (FTIR) and a corresponding Raman band at 1720 cm^{-1} are assigned to ν(C = O) stretching vibration, with PED contributions of 88–91%, confirming strong carbonyl character. The band observed at 1665 cm^{-1} in both FT-IR and Raman spectra is attributed to ν(C = N) stretching or mixed vibrational modes involving N–H bending and intermolecular interactions, with PED contributions of 60–75%, indicating vibrational coupling. These assignments are consistent with reported studies.

Aromatic Ring Vibrations

The FT-IR bands observed at 1595 cm^{-1}, 1565 cm^{-1}, and 1476 cm^{-1} align well with the Raman bands at 1590 cm^{-1}, 1560 cm^{-1}, and 1470 cm^{-1}, assigned to aromatic ν(C = C) stretching vibrations. PED contributions of 70–85% confirm that these modes are dominated by ring skeletal motions. The splitting of these bands indicates substitution effects and vibrational coupling within the aromatic framework.

C–H Deformation and Ring Vibrations

The bands at 979 cm^{-1} and 918 cm^{-1} (FT-IR) correspond to in-plane C–H bending vibrations, while Raman bands at 970 cm^{-1} and 910 cm^{-1} support these assignments. The out-of-plane C–H bending vibrations observed at 832 cm^{-1}, 761 cm^{-1}, 709 cm^{-1}, and 690 cm^{-1} (FT-IR) are also confirmed by Raman peaks in similar regions. These modes exhibit PED contributions of 40–70%, indicating mixed vibrational character and sensitivity to substitution patterns on the aromatic ring.

3.4. Optical studies

The Analysis of UV–Visible spectroscopy provides profound insights into the complex interplay among the electronic bandgap, atomic structure, and crystalline characteristics of the material under investigation. Our comprehensive absorption studies of the synthesised compound spanned a wide wavelength range from 200 to 1200 nm, providing a detailed exploration of its optical properties. The absorption spectrum, depicted in Fig. 9, shows a notably lower cutoff wavelength at 270 nm, indicating a significant transition. Beyond this threshold, the material showcases a striking absence of absorption, emphasising its fundamentally transmissive nature [37]. This characteristic highlights the necessity for materials with pronounced nonlinear optical (NLO) behaviours, which are essential for advanced optical applications.

Furthermore, the optical bandgap, calculated from the UV–Vis absorbance data, is presented in Fig. 9 **(inset)**. A plot of energy (hν) versus $(\alpha h\nu)^{1/2}$ indicates an optical bandgap of 4.5 eV. This value notably underscores the material's exceptional optical attributes. The substantial bandgap observed can be attributed to the intricate electronic structure of the compound, which is characterised by rigid aromatic rings and significant hydrogen bonding interactions, specifically, N–H···O and O–H···O—among the phenylglycinium cations and bromide anions. The combination of a high optical bandgap and a minimal absorption profile in the near-infrared region positions this material as a highly promising candidate for various applications in nonlinear optics [38].

In the realm of Photoluminescence studies, the captivating interplay between light and the electronic states of solid materials unveils an array

Table 4
Theoretical and Experimental vibrational wavenumbers (cm^{-1}) of DPGBr.

Exp. FTIR	Exp. FT Raman	Theo. Freq	Frequencies	IR Intensity	Raman Activity	PED
-	-	29	30	8.6425	0.7179	τHNCC (86)
-	-	37	38	0.9554	6.1805	τNCCC (88)
-	-	64	66	7.1807	0.9373	τOCCN (37)+β HNC (15)+β BrHN (38)
-	70	70	73	2.5005	1.2306	τOCCN (37)+β BrHN (24)
-	103	106	110	2.4435	4.5961	βCCC (24)+ϕ CCCC (38)+α NC(32)
-	-	167	173	4.5687	0.6016	αBrN (20)+β CCC (29)+ϕ CNCC (21)
-	220	221	229	16.9795	1.4815	αBrN (25)+β OCC (14)+β CCC(14)
-	-	279	288	2.0947	11.0371	τHNHBr (14)+τ HNHBr (31)+β HNBr (28)
-	304	302	312	44.1316	0.7823	βOCC (11)+β CCC (17)+α BrN(36)
-	-	335	347	13.8778	2.0126	τCCCC (18)
-	-	363	375	31.4276	3.2963	βOCC (25)+β CCC (14)+ϕ CNCC (12)
442	444	444	459	0.5574	0.1371	τHCCC (11)+τ HCCC (12)+τ CCCC (19)+τ CCCC (24)+τ CCCC (20)
-	-	485	502	49.205	1.8376	βOCO (15)+β OCC(26)
514	515	512	529	24.0946	0.9308	τHOCC (20)+ϕ OCOC (13)
604	604	602	622	119.6835	2.1512	τHOCC (32)+ϕ CCCC (14)
639	630	634	656	133.1244	3.8575	τHOCC (35)+β NCC(13)
-	649	655	678	8.471	7.8479	βOCO (22)+β CCC (17)+β CCC(13)
670	669	674	697	15.8445	3.7981	βOCO (26)+β CCC(16)
-	744	746	772	35.981	6.4939	ϕOCOC (21)+β CCC(24)
775	768	771	797	79.7193	0.077	τHCCC (11)+τ HCCC (14)
860	858	854	883	46.4852	1.9759	ϕCCCC (10)+τ HCCC (17)+τ HCCC (15)+τ HCCC (24)
875	877	876	906	23.8791	9.4319	βCCC (15)+ϕ OCOC (26)
-	-	936	968	29.8839	8.4085	αCC(31)
-	-	956	989	0.7615	0.1306	τHCCC (20)+τ HCCC (28)+τ HCCC (21)+τ HCCC (29)
1041	1040	1040	1076	38.8408	8.3934	αNC (26)+τ HCCC (16)+τ HCCC (18)+τ HCCC (16)
-	1057	1059	1095	0.7847	37.5705	βCCC (14)+β CCC (10)+α CC (14)+α CC(18)
1068	1071	1070	1107	46.2826	8.1001	αNC(32)
-	-	1094	1131	7.1981	4.2354	αCC (10)+α CC (13)+β CCC (29)+β HCC (11)+β CCC(15)
1108	1110	1106	1144	0.6148	0.6227	τHCCC (22)+τ HCCC (13)+τ HCCC (24)
-	1119	1125	1163	0.3643	0.2905	τHCCC (24)+τ HCCC (29)+τ

(*continued on next page*)

Table 4 (*continued*)

Exp. FTIR	Exp. FT Raman	Theo. Freq	Frequencies	IR Intensity	Raman Activity	PED
						HCCC (12)+τ CCCC (14)+
1160	1163	1157	1197	14.6944	0.3902	βHCC (14)+α CC (19)+α CC(17)
-	1188	1192	1233	197.8229	5.4515	αOC (23)+β HOC (36)+τ BrHNC (10)
-	-	1224	1266	80.8942	6.3931	βHCC (17)
1242	1242	1240	1283	23.6198	5.6138	αCC (11)+β HCC (15)+β HCC (11)+τ BrHNC (11)
1250	-	1252	1295	62.8386	8.1837	βHNBr (11)+β HNC (25)+
-	-	1288	1332	7.7137	5.9692	βHCC (11)+β HCC (20)+β HCC (16)+β HCC(14)
1294	1296	1292	1336	31.3101	11.472	αCC (16)+β HCC (13)+β HCC(10)
1326	1326	1328	1373	23.0911	1.845	βHCC (10)+β HCC (12)+α OC(11)
1402	1405	1400	1448	29.4687	1.2499	αOC (18)+β HOC (19)+β HCC(36)
-	-	1434	1483	21.4408	4.8759	βHCC (12)+β HCC (20)+τ HCCO (27)
1479	1480	1474	1525	6.2732	2.0144	βHCC (14)+τ HCCO (40)
-	-	1510	1561	53.5929	2.2731	αOC (14)+α CC (13)+β HCC(28)
1566	1567	1567	1621	14.8547	0.2382	βHCC (24)
1610	1609	1608	1663	14.3171	0.6925	βHCC (17)+β HCC (18)+β HCC

Table 4 (*continued*)

Exp. FTIR	Exp. FT Raman	Theo. Freq	Frequencies	IR Intensity	Raman Activity	PED
						(21)+β HCC(15)
1669	-	1668	1725	208.7224	37.2059	βHNBr (18)+β NHN (20)+β HNC (13)+β BrHN (20)+τ HNHBr (19)
-	-	1718	1776	2.9512	21.806	αCC (19)+α CC(23)
1730	1732	1728	1787	48.273	9.7681	βHNH (45)+τ HNHBr (15)+τ HNHBr (11)+τ BrHNC (11)
1745	-	1741	1800	0.3764	26.7836	αCC(29)
1772	-	1770	1831	85.758	4.6177	βHNBr (19)+β HNH (12)+τ HNHBr (27)+τ HNHBr (38)
1810	1807	1805	1866	329.35	9.2006	αOC(80)
2618	2619	2625	2715	2341.8101	366.8707	αNH(98)
3186	3179	3189	3298	16.3852	65.1103	αCH (100)
3258	-	3256	3367	13.0083	40.8467	αCH(91)
3277	-	3283	3395	1.5614	45.8285	αCH (24)+α CH (47)+α CH(18)
-	-	3293	3406	16.8446	78.7452	αCH (41)+α CH (23)+α CH(27)
-	-	3303	3416	16.6848	27.557	αCH (36)+α CH (11)+α CH (17)+α CH(34)
-	-	3316	3429	18.4407	243.5902	αCH (14)+α CH (41)+α CH (30)+α CH(12)
-	-	3551	3673	97.2698	59.5006	αNH (22)+α NH(78)
-	-	3652	3776	90.2061	25.5573	αNH (78)+α NH(22)
3863	-	3865	3997	175.6293	105.8182	αOH (100)

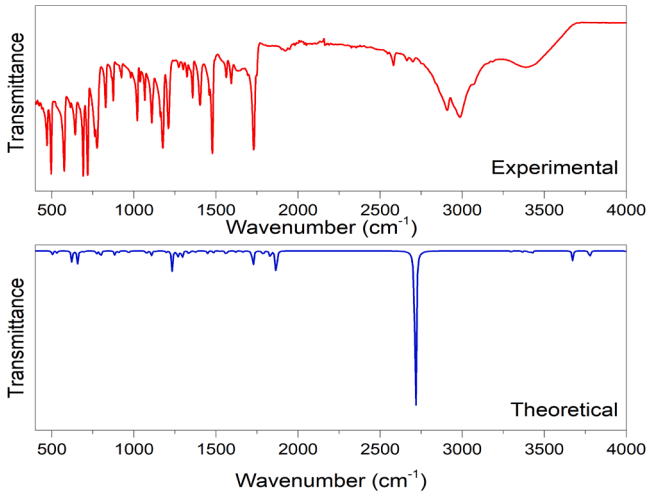

Fig. 8a. The experimental and calculated (theoretical) FT-IR spectrum of DPGBr.

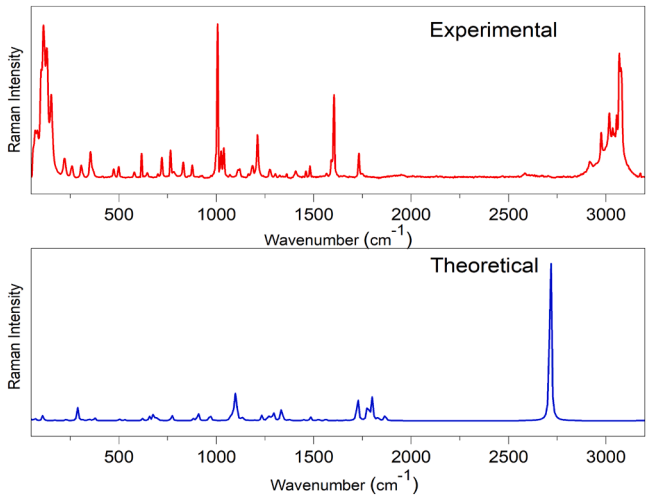

Fig. 8b. The experimental and calculated (theoretical) FT-Raman spectrum of DPGBr.

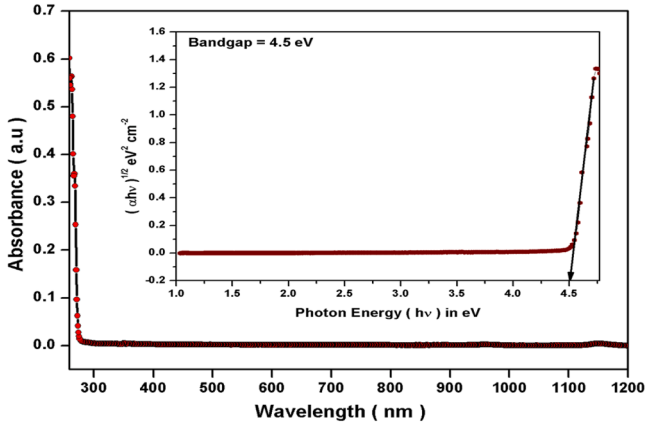

Fig. 9. UV–Vis-NIR absorbance spectrum and Tauc's plot (inset) of DPGBr.

of intriguing phenomena. For our analysis, we employed the state-of-the-art Fluorolog-3–11 spectrometer to assess the photoluminescence of the synthesised substance. This sophisticated device uses a powerful 450-watt xenon lamp to achieve an impressive 0.2 nm resolution, enabling highly detailed spectral measurements. The synthesised sample was effectively excited at a wavelength of 260 nm, generating a photoluminescent (PL) emission spectrum that is vividly illustrated in Fig. 10. Notably, in the near-violet region of the spectrum, we observed strong emissions characterised by prominent peaks at 290 nm and 310 nm. Beyond 310 nm, these peaks exhibited a rapid decline, indicating a critical threshold in the material's emission behaviour. The observed luminescence can be attributed to the radiative recombination of electron-hole pairs, as well as transitions involving localized states situated near the conduction band edge.

Furthermore, the incorporation of aromatic phenyl rings into the molecular structure likely enhances the π-π* transitions, contributing to the material's luminescent properties. However, the challenge is compounded by shallow trap states arising from minor defects within the crystal structure. This intricate relationship highlights the necessity of optimizing the synthesis conditions to improve the material's properties effectively. The results obtained indicate that the synthesized DPGBr material demonstrates the capability of generating near-violet fluorescence, suggesting promising applications in advanced photonic technologies. Such findings could pave the way for innovative solutions in various optoelectronic applications [39,40].

3.5. *Frontier molecular orbital analysis*

Frontier molecular orbital (FMO) analysis provides insights into the electronic properties and chemical reactivity [41]. Fig. 11. displays the HOMO-LUMO diagram for DPGBr. The global reactivity descriptors were calculated using Koopmans' theorem with the following standard equations:

Ionization potential: $I = -E_{HOMO}$
Electron affinity: $A = -E_{LUMO}$
Global hardness: $\eta = (I - A) / 2$
Chemical potential: $\mu = -(I + A) / 2$
Global softness: $S = 1 / (2\eta)$
Electrophilicity index: $\omega = \mu^2 / (2\eta)$

The calculated energies of the highest occupied molecular orbital (HOMO) and lowest unoccupied molecular orbital (LUMO) are 1.66 eV and –2.755 eV, respectively, yielding an energy gap of 4.415 eV, in good agreement with the experimental band gap of 4.5 eV This relatively large energy gap indicates that DPGBr is kinetically stable and exhibits low chemical reactivity. The ionization energy and electron affinity, derived from the HOMO and LUMO energies, are 1.66 eV and 2.755 eV, respectively. The chemical potential (–2.208 eV) suggests the system's stability, while the positive global hardness (0.548 eV) indicates resistance to charge transfer. The global softness (0.913 eV^{-1}) reflects

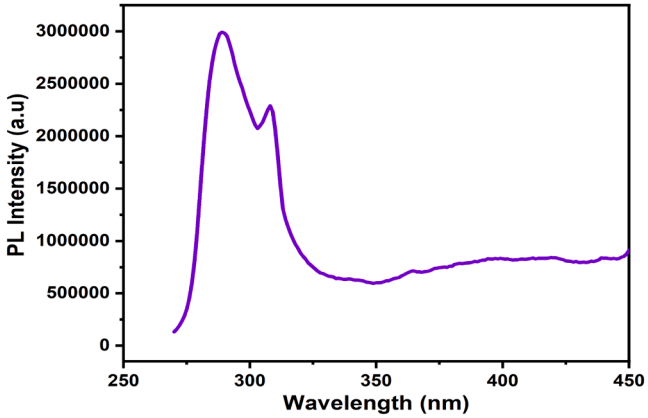

Fig. 10. PL spectrum of DPGBr.

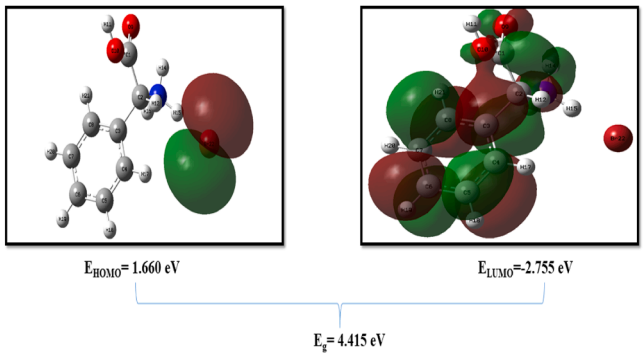

Fig. 11. HOMO-LUMO diagram of DPGBr.

moderate reactivity, and the electrophilicity index (4.45 eV) confirms the molecule's ability to accept electrons. The frontier molecular orbitals (HOMO and LUMO) provide important insight into the electronic structure and charge transfer behaviour of the molecule. The HOMO is mainly localised over the electron-rich regions of the molecule, particularly the phenyl ring and associated functional groups, indicating its role as the electron-donating part. In contrast, the LUMO is distributed over the electron-deficient regions, including the bromide ion and the nearby molecular framework, suggesting its electron-accepting nature. This spatial separation confirms the presence of intramolecular charge transfer (ICT), which is important for its optical and nonlinear optical (NLO) properties.

3.6. Molecular electrostatic potential

It reveals a uniquely anisotropic electrostatic environment that profoundly influences intermolecular recognition, charge migration, and molecular orientation within the crystalline structure [42]. As illustrated in Fig. 12, the MESP diagram shows a complex landscape in which the lowest region, marked by the most pronounced negative potential, surrounds the bromide anion. This area acts as a vital electronic reservoir, serving as the primary target for electrophilic probes due to its high electron density.

Secondary negative regions are prominently located around the lone-pair sites of oxygen and nitrogen within the organic moiety, indicating that these heteroatoms may interactively compete with Br^- to act as hydrogen bond or electron acceptors. Conversely, the most pronounced maxima on the map are observed on the hydrogen atoms attached to the amine group and, to a lesser extent, on specific CH sites of the phenylglycinium cation. These maxima highlight the regions that serve as preferred hydrogen-bond donors, revealing the directional nature of N–H···Br and N–H···O interactions within the lattice. Furthermore, the localised negative potential around the oxygen atoms indicates the intriguing possibility of bifurcated or cooperative hydrogen-bonding motifs. In such cases, a single N–H donor could simultaneously interact with both the bromide anion and an oxygen-accepting group, potentially enhancing the stability of the crystal lattice. This complex and dynamic interplay of electrostatic forces not only contributes to the crystal's structural integrity but also opens avenues for exploring remarkable properties and reactivity patterns. Such cooperative interactions could be crucial in the innovative design of new materials with precisely tuned functionalities.

3.7. Hirshfeld surface analysis

The analysis reveals a fascinating interplay of intermolecular forces that is essential to its crystal packing. Notably, hydrogen-bonding interactions with the bromide counterion, along with numerous van der Waals contacts, are crucial for stabilising the overall structure [43]. Fig. 13 vividly illustrates the dnorm surface, shape index, and curvedness of DPGBr, while Fig. 14 presents the detailed 2D fingerprint plot. The dnorm surface, displayed against the normalised contact distance, highlights striking red regions indicating the N–H···Br and O–H···Br interactions. These intense red points confirm the importance of these hydrogen bonds, as they represent the shortest and most vital intermolecular contacts within the crystal structure. Moreover, the shape index and curvedness maps reveal localised red and blue features, along with widespread regions of low curvedness, which likely correspond to C–H··π interactions and subtle π···π stacking between the aromatic phenyl rings. This indicates that while hydrogen bonds with halides primarily determine structural directionality, aromatic contacts also help maintain the framework's overall stability. The parameters di and de represent the distances from a point on the Hirshfeld surface to the nearest atom inside and outside the surface, respectively. Specifically, di (internal distance) corresponds to the distance from the surface to the nearest nucleus within the molecule, while de (external distance) refers to the distance to the nearest nucleus of a neighbouring molecule. These parameters are used to generate two-dimensional fingerprint plots, which provide detailed information about intermolecular interactions and contacts within the crystal structure. The two-dimensional fingerprint plots provide quantitative insight into the intermolecular interactions governing the crystal packing. The overall fingerprint map shows a combination of sharp spikes and broad regions, indicating the presence of both specific directional interactions and dispersive contacts. The H···H interactions contribute the highest percentage (30.3%), reflecting dominant van der Waals interactions within the crystal. These

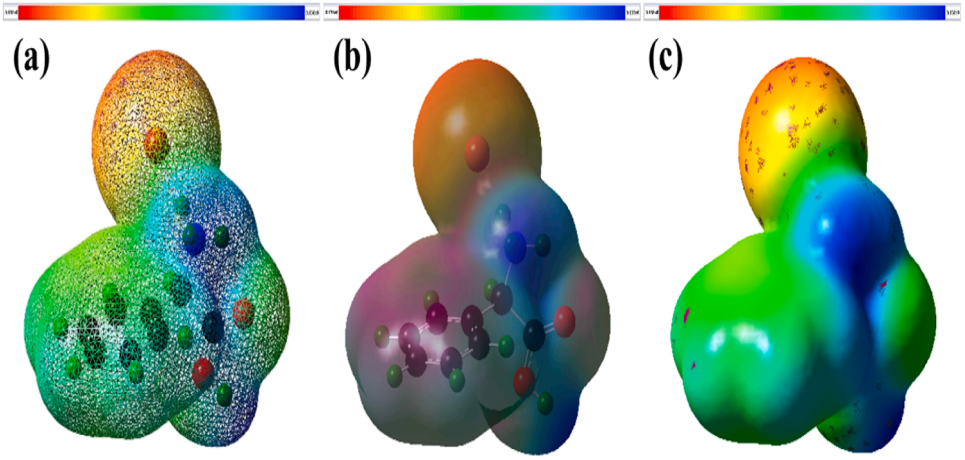

Fig. 12. (a) Mesh (b) Transparent (c) Solid MESP diagram of DPGBr.

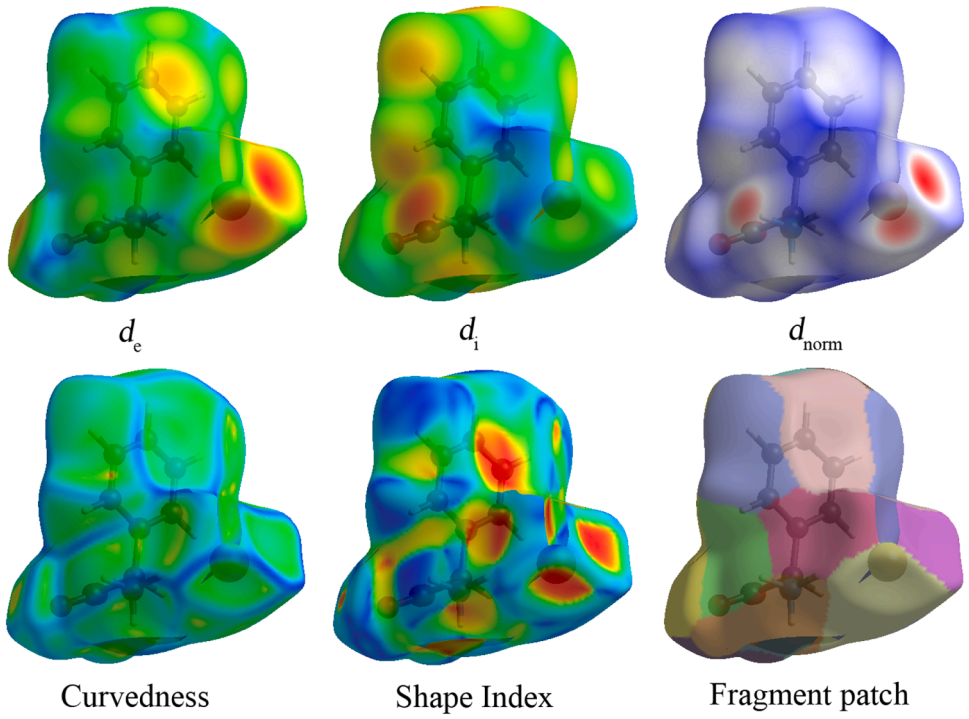

Fig. 13. dnorm, Shapeindex and Curvedness of DPGBr.

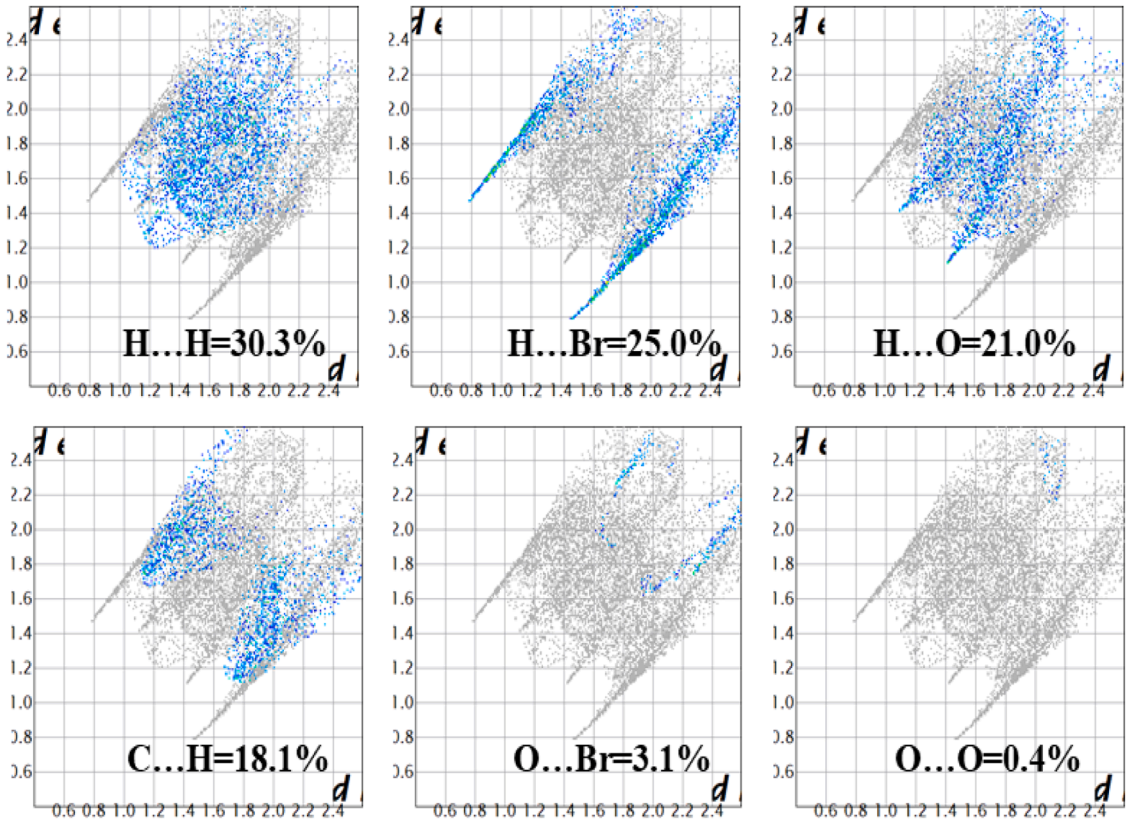

Fig. 14. 2D Fingerprint plot of DPGBr.

contacts form the background of the packing and indicate that weak hydrogen-based interactions play a major role in stabilizing the structure. The H···Br contacts (25.0%) appear as distinct sharp spikes in the fingerprint plot, suggesting significant hydrogen bonding or close contacts involving bromine atoms. These interactions indicate that bromine acts as an important acceptor site, contributing to directional stabilisation of the crystal lattice. Similarly, the H···O interactions (21.0%) exhibit well-defined spikes, characteristic of classical or

non-classical hydrogen bonding. These interactions highlight the role of oxygen atoms as strong electronegative centres participating in intermolecular bonding. The C···H interactions (18.1%) represent weak C–H···π or C–H···C contacts, contributing to additional stabilisation through dispersive forces and weak hydrogen bonding. In contrast, O···Br (3.1%) and O···O (0.4%) interactions are rare and play a negligible role in the overall crystal packing. These compelling results bolster the credibility of the crystallographic model, underscoring the strength of the compound's directional interactions. This complex tapestry of intermolecular interactions not only fortifies the structural integrity of DPGBr but also influences its material properties. Such characteristics point to promising applications in various fields, including catalysis and drug design. Moreover, these supramolecular assemblies suggest exciting new avenues for optimising the performance of diverse fabrication devices, heralding potential advancements in material science and engineering. To provide a clearer understanding of intermolecular interactions, the percentage contributions of different contacts obtained from the Hirshfeld surface analysis are summarized in Table 5. The analysis reveals that H···H interactions contribute the highest percentage, followed by H···Br/Br···H and O···H/H···O contacts. Minor contributions arise from C···H/H···C, O···Br/Br···O, and C···Br/Br···C interactions. These results highlight the dominance of hydrogen bonding and van der Waals interactions in stabilizing the crystal structure.

3.8. Thermal analysis

The thermal behaviour of DPGBr was investigated using a NETZSCH STA 409C/CD thermal analyser. Differential thermal analysis (DTA) and thermogravimetric analysis (TG) were employed to examine phase transitions and decomposition characteristics [44]. The measurements were carried out over a temperature range of 40–600 °C at a heating rate of 10 K/min under a nitrogen atmosphere. The TG–DTA curves are presented in Fig. 15. The TGA profile reveals that the compound undergoes decomposition in two major stages. The initial mass of the sample was 1.9150 mg. The first stage of decomposition, with a weight loss of 41.12%, is attributed to the elimination of volatile species, predominantly hydrogen bromide (HBr), along with partial degradation of the protonated amino acid moiety. The presence of bromide ions and protonated amine groups in the structure supports the evolution of HBr at elevated temperatures. This stage may also involve concurrent decarboxylation and deamination processes, resulting in intermediate fragments.

The second stage exhibits a significant mass loss of 57.60%, corresponding to the complete decomposition of the remaining organic framework. This includes the breakdown of the phenyl ring and associated molecular backbone, leading to the formation of gaseous products such as CO_2, NH_3, and hydrocarbon fragments, with negligible residue remaining. The DTA curve displays a sharp endothermic peak at 235 °C, which is assigned to the melting point of the crystal. This well-defined peak indicates good crystallinity of the sample. A subsequent endothermic feature observed at higher temperatures is attributed to the volatilisation and decomposition of the material. The TG–DTA results demonstrate that DPGBr is thermally stable up to its melting point, after which it undergoes systematic thermal decomposition. These observations are consistent with the TG/DTA findings and confirm the material's structural integrity up to 235 °C [45].

Table 5
Percentage Contribution of Intermolecular Contacts from Hirshfeld Surface Analysis.

Interaction Type	Contribution (%)
H···H	30.3
H···Br / Br···H	25.0
O···H / H···O	21.0
C···H / H···C	18.1
O···Br / Br···O	3.1
O···O / O···O	0.4

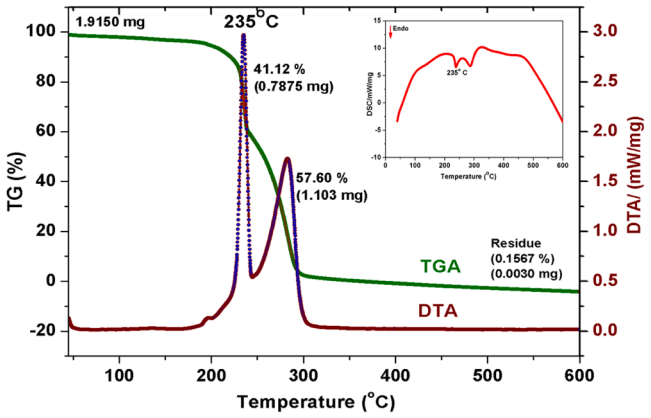

Fig. 15. TG-DTA spectrum and DSC spectrum (inset) of DPGBr.

3.9. Hyperpolarizability

The interrelationships among nonlinear optical properties, photocurrent generation, and molecular structure were analysed using the B3LYP/6–31++G(d,p) POLAR basis set, in conjunction with the finite-field method, to calculate the polarizability and hyperpolarizability of DPGBr. The x, y, and z components were employed to define the total static dipole moment (μ_0), the anisotropy of the polarizability ($|\alpha_0|$), the mean polarizability ($\Delta\alpha$), and the overall first hyperpolarizability (β_0).

$$\mu_0 = (\mu_x^2+\mu_y^2+\mu_z^2)^{1/2}$$
$$|\alpha_0| = 1/3(\alpha_{xx}+\alpha_{yy}+\alpha_{zz})$$
$$\Delta\alpha = 2^{-1/2}[(\alpha_{xx}-\alpha_{xx})^2+(\alpha_{yy}-\alpha_{zz})^2+(\alpha_{zz}-\alpha_{xx})^2]^{1/2}$$
$$\beta_0 = [(\beta_{xxx}+\beta_{xyy}+\beta_{xzz})^2+(\beta_{yyy}+\beta_{xxy}+\beta_{yzz})^2+(\beta_{zzz}+\beta_{xxz}+\beta_{yyz})^2]^{1/2}$$

The calculated polarizability (α_o) and first-order hyperpolarizability (β_o) values obtained from Gaussian 09 W are expressed in atomic units (a.u.) and were converted into electrostatic units (esu) using standard conversion factors (1 a.u. of $\alpha = 0.1482 \times 10^{-24}$ esu and 1 a.u. of $\beta = 8.6393 \times 10^{-33}$ esu). All reported values in this work are presented in esu units for consistency with the literature. This ensures proper comparison with previously reported nonlinear optical (NLO) materials. The x, y, and z values of α_o and β_o were used as the zero points in the output of Gaussian 09 w. The value of β_o is an important parameter for evaluating the efficiency of the NLO system. The α_o and β_o values of the DPGBr molecule are 2.63×10^{-23} esu and 2.24×10^{-22} esu, respectively. To evaluate the nonlinear optical efficiency, the calculated β_o value for DPGBr (2.24×10^{-22} esu) was compared with those of standard reference materials. The β_o value of Urea is about 0.372×10^{-30} esu, while Potassium dihydrogen phosphate shows relatively lower hyperpolarizability. The β_o value of DPGBr is much higher than that of urea, indicating strong nonlinear optical behaviour. A comparison with similar amino acid-based NLO materials also shows that DPGBr has a comparatively higher β_o value. This enhancement is mainly due to strong donor–acceptor interactions and intramolecular charge transfer within the molecule. These results confirm that DPGBr exhibits good nonlinear optical properties and is suitable for photonic and optical limiting applications. Table 6 presents the precise values of polarizability and hyperpolarizability. These findings are significant for understanding how molecular structure influences the optical properties of materials and may provide insights into potential applications in photonic devices and other NLO technologies.

3.10. Nonlinear optical analysis

The compound's second-harmonic generation (SHG) efficiency was

Table 6
Calculated Polarizability and Hyperpolarizability values of DPGBr.

Polarizability		Hyperpolarizability	
α_{xx}	198.8681	β_{xxx}	93.87057
α_{xy}	−1.6983	β_{xxy}	−17.9926
α_{yy}	153.7994	β_{xyy}	73.86277
α_{xz}	4.6987	β_{yyy}	−41.6136
α_{yz}	−23.8948	β_{xxz}	−163.586
α_{zz}	180.2106	β_{xyz}	18.9035
		β_{yyz}	−43.0454
		β_{xzz}	137.3377
		β_{yzz}	4.482654
		β_{zzz}	−249.638

evaluated using the Kurtz-Perry powder method [46]. A Q-switched Nd: YAG laser at 1064 nm, operating at 4.1 mJ with an 8 ns pulse width and a 10 Hz repetition rate, was used as the light source. The compound was ground into a fine powder to ensure uniform particle size. Second-harmonic signals were generated under laser irradiation, as indicated by the bright green emission detected by a photomultiplier tube. The SHG results were systematically compared with those of conventional potassium dihydrogen phosphate (KDP). The material exhibited an SHG efficiency 1.2 times greater than that of standard KDP. Additionally, the compound's ability to generate second-harmonic light increased with larger particle sizes [47].

The non-centrosymmetric material under investigation exhibits notable second- and third-order nonlinear optical properties, highlighting its significant potential in advanced optical applications [48]. The Z-scan technique, developed by Bahae [49], is used to evaluate the efficiency of third-order NLO responses. A Q-switched Nd: YAG laser operating at 532 nm with a pulse width of 9 nanoseconds at a repetition rate of 10 Hz. The resulting data clearly display characteristic peaks and valleys, indicating NLO response at higher levels. Conversely, the shoulder features observed at lower intensities reflect the material's linear transmittance, emphasising the material's optical response diversity. This unique trait suggests the material can effectively withstand higher light intensities, making it especially useful for various photonic applications. Table 7 provides a comprehensive overview of the calculated third-order nonlinear optical parameters for DPGBr, highlighting its remarkable properties. Fig. 16 presents the OA curve, showing normalised transmission values calculated from Eq. (1), offering further insight into the material's distinctive optical characteristics.

$$T(z) = \frac{1}{\sqrt{\pi q(z)}} \int_{-\infty}^{+\infty} \ln\left[1 + q(z)\exp\left(-\tau^2\right)\right] d\tau \quad (1)$$

where $q(z) = \beta L_{eff} \frac{I_o}{\left(1+\left(\frac{z}{z_o}\right)^2\right)}$, β is the nonlinear absorption coefficient, Zo is the Rayleigh range or diffraction length, I_o is the input intensity of the laser beam, and L_{eff} is the effective length of the sample. The nonlinear absorption characteristics observed in DPGBr arise from the fascinating phenomenon of two-photon absorption (2PA), with both theoretical models and experimental results showing remarkable agreement. In this study, a focused laser beam was precisely directed to achieve a waist of 16.9 μm using a lens with a focal length of 15 cm, resulting in a Rayleigh range of 1.69 mm. The result was a remarkable V-shaped characteristic on the optical absorbance (OA) Z-scan curve,

Table 7
Third-order NLO parameters of DPGBr.

Crystal	Saturation Intensity, Isx 10^{11} W/m^2	Nonlinear Absorption Coefficient, β x 10^{-10} m/W	Onset Optical Limiting Threshold, x 10^{12} W/m^2
DPGBr	80	0.48	6.24

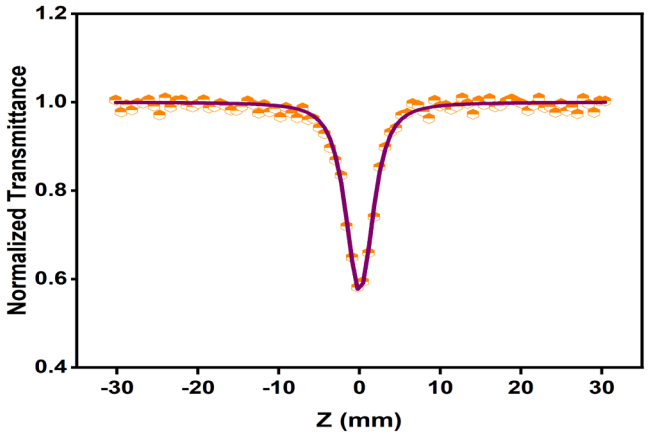

Fig. 16. Open aperture (OA) curve of DPGBr.

perfectly aligned with the focal point (Z = 0). This observation indicates reverse saturable absorption (RSA), a fascinating nonlinear absorption phenomenon. In this behaviour, the probability of absorption in excited states exceeds that in the ground state, leading to a pronounced decrease in transmittance as the light intensity increases. This interplay of excitation and absorption creates a striking visual and analytical signature in the data, highlighting the intriguing complexities of light-matter interaction at elevated intensities.

Such RSA attributes are characteristically linked with 2PA processes. The intricate extended π-conjugation in the phenylglycine moiety of DPGBr is notably augmented by the presence of various functional group donors (amino) and acceptors (carboxylate and bromide), which together facilitate a phenomenon known as intramolecular charge transfer (ICT). This interaction promotes substantial electronic delocalisation, thereby significantly increasing the propensity for nonlinear photon absorption under intense laser excitation.

To analyse the experimental data, a standard 2PA model was employed, which allowed for the precise fitting of results and yielded a nonlinear absorption coefficient (β) of approximately 0.48×10^{-11} m/W. This finding further corroborates the effective 2PA nature exhibited by DPGBr. Moreover, the marked dip observed in the OA curve reflects a noteworthy modulation of energy-dependent absorption, a clear indicator of the material's strong nonlinear optical (NLO) activity. The complementary optical limiting (OL) curve, Fig. 17, reinforces these observations. With increasing input intensity, the normalised transmittance remains almost constant until it undergoes a sharp decline at a critical intensity, the optical limiting threshold, which is observed at around 6.24×10^{12} W/m^2. This significant drop in transmittance demonstrates DPGBr's ability to effectively block high-intensity laser light.

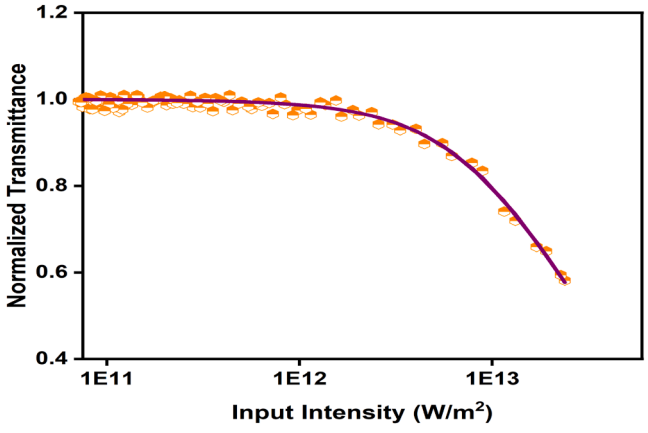

Fig. 17. Optical limiting (OL) curve of DPGBr.

This mechanism is predominantly driven by excited-state absorption coupled with 2PA-induced RSA, which becomes increasingly influential at higher fluences. The synergistic effects of robust RSA, a moderate β value, and a low optical-limiting threshold position make DPGBr a strong candidate for optical applications, especially in photonics and laser protection [50,51].

4. Conclusion

D-Phenylglycinium bromide (DPGBr) single crystals have been successfully synthesised by slow evaporation and systematically characterised to elucidate their structural and optical properties. Single-crystal X-ray diffraction (XRD) analysis confirms the presence of an orthorhombic non-centrosymmetric structure, in which hydrogen bonding is pivotal for lattice stabilisation. The excellent concordance between experimental data and density functional theory (DFT) results enhances the reliability of the molecular model. Fourier-transform infrared (FT-IR) spectroscopy further validates the vibrational assignments, while optical investigations indicate a substantial transparency window with a band gap of approximately 4.5 eV. The relatively large HOMO–LUMO gap signifies molecular stability. Hirshfeld surface and molecular electrostatic potential (MESP) analyses underscore the significance of intermolecular interactions in determining crystal packing arrangements. Thermal studies indicate structural stability up to 235 °C, and energy-dispersive X-ray spectroscopy (EDX) confirms the compound's purity. The observed reverse saturable absorption and quantifiable nonlinear absorption coefficient illustrate effective third-order nonlinear optical behaviour, indicating that DPGBr presents a promising candidate for applications in optical limiting and photonic devices.

Declaration statement

All authors reviewed the manuscript and accepted it for publication.

Ethical approval

All experiments were carried out in accordance with university guidelines. None of the authors used human beings as research subjects.

Consent for publication

In the present study, there were no person's data in any form.

Funding declaration statement

The authors did not receive any financial support from any organisation for the submitted work.

CRediT authorship contribution statement

P Hemalatha: Writing – original draft, Methodology, Data curation, Conceptualization. **M Mohanraj:** Writing – review & editing, Validation, Methodology, Data curation. **S Anandhi:** Writing – review & editing, Validation, Formal analysis, Data curation. **H Jemmy Chirsty:** Writing – review & editing, Validation, Formal analysis, Data curation. **T C Sabari Girisun:** Writing – review & editing, Validation, Formal analysis, Data curation. **M Parthasarathy:** Validation, Supervision, Methodology, Investigation, Data curation.

Declaration of competing interest

The authors declare that they have no known competing financial interests or personal relationships that could have appeared to influence the work reported in this paper.

Acknowledgement

The authors sincerely thank Vels Institute of Science, Technology and Advanced Studies (VISTAS), Pallavaram, Chennai-600117, for supporting this research. We also appreciate the valuable contributions of SAIF and IIT-Madras for their assistance with structural refinement and with Single-crystal XRD, UV-visible-NIR, Photoluminescence, EDAX, and TG-DTA/DSC analyses.

Data availability

Data will be made available on request.

References

[1] S. Shalini, S.S. Kirupavathy, M.I.S. Kumar, Growth and characterisation of a third-order nonlinear optical crystal 4-dimethylamino pyridinium p-bromophenolate, J. Mol. Struct. 1224 (2021) 129078, https://doi.org/10.1016/j.molstruc.2020.129078.
[2] A. Subashini, R. Kumaravel, S. Leela, H.S. Evans, D. Sastikumar, K. Ramamurthi, Synthesis, growth and characterisation of 4-bromo-4′chloro benzylidene aniline – a third order nonlinear optical material, Spectrochim. Acta - Mol. Biomol. Spectrosc. 78 (2011) 935–941, https://doi.org/10.1016/j.saa.2010.11.041.
[3] L. Poornima, R.S. Babu, S. Kalainathan, A new stilbazolium family crystal of 1-methyl-2-[2-(3-nitro-phenyl)-vinyl]-pyridinium iodide (MNPI): investigation of the growth, structural, optical, surface and third-order nonlinear optical properties, J. Mol. Struct. 1280 (2023) 134976, https://doi.org/10.1016/j.molstruc.2023.134976.
[4] P. Karuppasamy, V. Sivasubramani, M.S. Pandian, P. Ramasamy, Growth and characterisation of semi-organic third-order nonlinear optical (NLO) potassium 3,5-dinitrobenzoate (KDNB) single crystals, RSC Adv 6 (2016) 109105–109123, https://doi.org/10.1039/C6RA21590D.
[5] P. Jayaprakash, P. Sangeetha, M. Peer Mohamed, G. Vinitha, S. Muthu, M. Prakash, M. Lydia Caroline, Growth and characterisation of DL-mandelic acid (C6H5CH (OH)CO2H) single crystal for third-order nonlinear optical applications, J. Mol. Struct. 1148 (2017) 314–321, https://doi.org/10.1016/j.molstruc.2017.07.049.
[6] M.K. Kumar, S. Sudhahar, P. Pandi, G. Bhagavannarayana, R.M. Kumar, Studies of the structural and third-order nonlinear optical properties of solution-grown 4-hydroxy-3-methoxy-4′-N′-methylstilbazolium tosylate monohydrate crystals, Opt. Mater. (Amst.) 36 (2014) 988–995, https://doi.org/10.1016/j.optmat.2014.01.007.
[7] S. Chandrasekar, E. Manjula, S. Nandhini, G. Vinitha, P. Murugakoothan, A comprehensive study on synthesis, growth and characterisation of guanidinium 4-chloro-3-nitrobenzoate monohydrate (G4C3NBM) single crystal for NLO applications: a third-order nonlinear optical material, J. Mol. Struct. 1296 (2024) 136837, https://doi.org/10.1016/j.molstruc.2023.136837.
[8] A. Antony Raj, R. Gunaseelan, P. Sagayaraj, Investigation on third-order nonlinear optical, electrical and surface properties of organic stilbazolium crystal of 4-N, N-dimethylamino-N′-methylstilbazolium p-methoxybenzenesulfonate, Opt. Mater. (Amst.) 38 (2014) 102–107, https://doi.org/10.1016/j.optmat.2014.10.011.
[9] S.J. Sundaram, J.V. Ramaclus, M. Panneerselvam, M. Jaccob, P. Antony, L. Anandaraj, S. Muthupandi, A.J.P. Paul Winston, P. Sagayaraj, Crystal growth and characterisation of 4-[4-(4-dimethylamino-phenyl) buta-1,3-dienyl]-1-methyl pyridinium iodide for higher order non-linear applications, Opt. Laser Technol. 121 (2020) 105831, https://doi.org/10.1016/j.optlastec.2019.105831.
[10] P. Antony, S.J. Sundaram, J.V. Ramaclus, S. Antony Inglebert, A. Antony Raj, S. Dominique, T.A. Hegde, G. Vinitha, P. Sagayaraj, Synthesis, growth, crystal structure, thermal, linear and nonlinear opticalanalysis of new extended π-conjugated organic material based on methyl pyridinium compound of 4-(4-(4-(dimethylamino) phenyl) buta-1,3-dienyl)-1-methylpyridinium p-styrenesulfonate, J. Mol. Struct. 1196 (2019) 699–706, https://doi.org/10.1016/j.molstruc.2019.07.024.
[11] T. Murugan, S. Suresh, B.M. Boaz, Studies on the growth and characterisation of a new organic nonlinear optical single crystal: 2-amino 5-methyl-pyridinium 4-methoxybenzoate for optoelectronic and photonic devices, Opt. Mater. (Amst.) 136 (2023) 113379, https://doi.org/10.1016/j.optmat.2022.113379.
[12] S. Ravi, R. Sreedharan, K.R. Raghi, T.K. Manoj Kumar, K. Naseema, Linear–nonlinear optical and quantum chemical studies on quinolinium 3,5-dinitrobenzoate: a novel third-order non-linear optical material for optoelectronic applications, Spectrochim. Acta - Mol. Biomol. Spectrosc. 249 (2021) 119304, https://doi.org/10.1016/j.saa.2020.119304.
[13] S.S. Sundari, M. Mehala, N. Arunadevi, P. Kanchana, S.S. Alharthi, E.R. Kumar, Y. Al-Douri, A.F.A. El-Rehim, Structural and optical properties of salicyl-N-methyl-4-stilbazolium tosylate: thermal, DFT, MEP and Hirshfeld surface analysis, J. Mol. Struct. 1271 (2023) 134072, https://doi.org/10.1016/j.molstruc.2022.134072.
[14] S. Karthigha, S. Kalainathan, Crystal growth, structural investigation and characterisation of newly grown quinolinium derivative single crystal: 1-ethyl-2-(2-p-tolyl-vinyl)-quinolinium; iodide, J. Cryst. Growth 453 (2016) 77–89, https://doi.org/10.1016/j.jcrysgro.2016.08.012.
[15] K. Senthil, S. Kalainathan, A.R. Kumar, Growth and characterisation of an organic single crystal: 2-[2-(4-Diethylamino-phenyl)-vinyl]-1-methyl-pyridinium iodide,

Spectrochim. Acta - Mol. Biomol. Spectrosc. 125 (2014) 335–344, https://doi.org/10.1016/j.saa.2014.01.109.
[16] A. Satyam, M.D. Hocker, K.A. Kanemaguire, A.S. Morgan, H.O. Villar, M.H. Lyttle, Structure–activity relationship studies of novel ligands targeting biological receptors, J. Med. Chem. 39 (1996) 1736–1747, https://doi.org/10.1021/jm950668u.
[17] L.R. Jayasinghe, A. Datta, S.M. Ali, J. Zymunt, D.G. Vander Velde, G.I. Georg, Synthesis and characterisation of phenylglycine analogues with pharmacological potential, J. Med. Chem. 37 (1994) 2981–2984, https://doi.org/10.1021/jm00043a022.
[18] A. Boto, J.A. Gallardo, R. Hernandez, F. Ledo, A. Munoz, R.J. Murguia, M. Menacho-Marquez, A. Orjales, C.J. Saavedra, Design, synthesis and biological evaluation of halogenated phenylglycine derivatives, Bioorg. Med. Chem. Lett. 16 (2006) 6073–6077, https://doi.org/10.1016/j.bmcl.2006.08.065.
[19] J.L. Lynch, P. Honore, D.J. Anderson, W.H. Bunnelle, K.H. Mortell, C. Zhong, C. L. Wade, C.Z. Zhu, H. Xu, K.C. Marsh, C.-H. Lee, M.F. Jarvis, M. Gopalakrishnan, Pharmacological evaluation of L-phenylglycine analogues with gabapentin-like analgesic profiles, Pain 125 (2006) 136–142, https://doi.org/10.1016/j.pain.2006.06.015.
[20] G.B. McGaughey, M. Gagné, A.K. Rappé, Investigation of aromatic ring interactions in biological systems, J. Biol. Chem. 273 (1998) 15458–15463, https://doi.org/10.1074/jbc.273.25.15458.
[21] S. Ravichandran, J.K. Dattagupta, Chandana Chakrabarti, D-Pphenylglycine hydrochloride, Acta Cryst. C 54 (1998) 499–501, https://doi.org/10.1107/S0108270197014674.
[22] K. Bouchouit, L. Bendheif, N. Benali-Cherif, D-phenylglycinium nitrate, Acta Cryst. E 60 (2004) 272–274, https://doi.org/10.1107/S1600536804000972.
[23] S. Ramaswamy, R.K. Rajaram, V. Ramakrishnan, Raman and IR spectral studies of D-phenylglycinium perchlorate, J. Raman Spectros. 33 (2002) 689–698, https://doi.org/10.1002/jrs.898.
[24] L. Gobinathan, K. Boopathy, Photoluminescence, laser damage threshold, optical transmittance, FTIR, mechanical, dielectric, thermal and XRD studies on bis – glycine hydrochloride single crystal, J. Advance. Chem. 12 (2016) 4523–4535.
[25] N. Srinivasan, B. Sridhar, R.K. Rajaram, Bis(D-phenylglycinium) sulfate monohydrate, Acta Cryst. E 57 (2001) 754–756, https://doi.org/10.1107/S1600536801011941.
[26] M. Parthasarathy, K. Arun Kumar, R. Gopalakrishnan, D-phenylglycinium bromide, Acta Cryst. E 69 (2013) 470, https://doi.org/10.1107/S1600536813004807.
[27] M. Parthasarathy, R. Gopalakrishnan, Growth, photoluminescence, thermal and mechanical behaviour of ethyltriphenylphosphonium bromide dihydrate crystal, Opt Mater. 35 (2013) 2056–2061, https://doi.org/10.1016/j.optmat.2013.05.007.
[28] G.M. Sheldrick, A short history of SHELX, Acta Crystallogr. A 64 (2008) 112–122, https://doi.org/10.1107/S0108767307043930.
[29] L.J. Farrugia, WinGX and ORTEP for windows: an update, J. Appl. Crystallogr. 32 (1999) 837–838, https://doi.org/10.1107/S0021889899006020.
[30] A. Frisch, A.B. Neilson, A.J. Holder, GaussView user manual, Gaussian, Pittsburgh, 2000.
[31] M.J. Frisch, et al., Gaussian-09, Revision A.01, Gaussian, Inc., Wallingford, CT, 2009.
[32] S. Kesharwani, B. Brauer, J.M.L. Martin, J. Chem. Phys. 142 (2015) 054110.
[33] L.J. Bellamy, Infrared Spectra of Complex Molecules, Chapman and Hall, London, 1980.
[34] Said Benramache, Yacine Aoun, Said Lakel, Boubaker Benhaoua, Chahrazed Torchi, The calculate of optical gap energy and urbach energy of $Ni_{1-x}Co_xO$ thin films, Sādhanā 44 (2019) 26, https://doi.org/10.1007/s12046-018-1003-y.
[35] S. Bendia, K. Ouari, S. Dekar, M. Merzougui, W. Benabid, R. Bourzami, Insights into β-diketone: a multi-faceted study from crystal structure to molecular docking and antioxidant potential, Russ. J. Phys. Chem. A 99 (2025) 1843–1858, https://doi.org/10.1134/S0036024425701250.
[36] S. Bendia, K. Ouari, B. Wafa, Design of a novel uranyl(VI) β-diketone complex: structural characterization, Hirshfeld surface analysis, electrochemical behavior and antibacterial evaluation, J. Mol. Struct. 1360 (2026) 145546, https://doi.org/10.1016/j.molstruc.2026.145546.
[37] M. Mohanraj, M. Parthasarathy, A comprehensive evaluation of nonlinear optical materials: synthesis, growth, spectral, photoluminescence, LDT, photoconductivity, thermal, antibacterial and second harmonic generation analysis, Solid State Commun. 404 (2025) 116113, https://doi.org/10.1016/j.ssc.2025.116113.
[38] M. Suriya, M. Manimaran, B.M. Boaz, Investigation on the optical, spectral, electrical, mechanical, and laser damage threshold studies of bis (4-acetylanilinium) tetrachloridozincate (B4ATCZ) crystal, J. Mater. Sci. 32 (2021) 11393–11417, https://doi.org/10.1007/s10854-021-05265-2.
[39] P. Hemalatha, M. Mohanraj, M. Lakshmipriya, T.C. Sabari Girisun, P. Jayaprakash, M. Parthasarathy, Theoretical and experimental studies on a semi-organic third-order nonlinear optical material for photonic and optical limiting applications, J. Mater. Sci. 36 (2025) 2147, https://doi.org/10.1007/s10854-025-16117-8.
[40] H.B. Schlegel, Optimization of equilibrium geometries and transition structures, J. Comput. Chem. 3 (1982) 214–218, https://doi.org/10.1002/jcc.540030212.
[41] P. Hohenberg, W. Kohn, Inhomogeneous electron gas, Phys. Rev. 136 (1964) B864–B871, https://doi.org/10.1103/PhysRev.136.B864.
[42] C. Lee, W. Yang, R.G. Parr, Development of the Colle–Salvetti correlation-energy formula into a functional of the electron density, Phys. Rev. B 37 (1988) 785–789, https://doi.org/10.1103/PhysRevB.37.785.
[43] Milica Tomasevic, Mira Anicic, Trace element content in urban tree leaves and SEM-EDAX characterisation of deposited particles, Phys., Chem. Technol. 8 (2010) 1–13, https://doi.org/10.2298/FUPCT1001001T.
[44] B. Uma, K. Sakthi Murugesan, S. Krishnan, R. Jayavel, B.Milton Boaz, Growth, optical, thermal and dielectric studies of a highly polarisable semi organic NLO crystal: bis D-phenyl glycinium sulphate monohydrate, Mater. Chem. Phys. 142 (2013) 659–666, https://doi.org/10.1016/j.matchemphys.2013.08.018.
[45] F. Yogam, I. Vetha Potheher, R. Jeyasekaran, M. Vimalan, M. Antony Arockiaraj, P. Sagayaraj, Growth, thermal, and optical properties of L-asparagine monohydrate NLO single crystal, J. Therm. Anal. Calorim. 114 (2013) 1153–1159, https://doi.org/10.1007/s10973-013-3138-8.
[46] Mengran Sun, Guili Wang, Jiyong Yao, The Kurtz–Perry powder technique revisited: a study of the effect of reference selection on powder second-harmonic generation response, Molecules 28 (2023) 1116, https://doi.org/10.3390/molecules28031116.
[47] K. Rajesh, P. Krishnan, A. Mani, K. Anandan, K. Gayathri, P. Devendran, Physical strength and opto-electrical conductivity of L-serine phosphate single crystal for structural and photonics devices fabrication, Mater. Res. Innovat. 24 (2020) 295–300, https://doi.org/10.1080/14328917.2019.1664178.
[48] H. Algarni, A.A. Alshahrani, A.E. Al-Salami, Improving structural, UV–visible, SHG efficiency, third-order nonlinear optical, mechanical, thermal and dielectric properties of ZTC crystal using π-bonded ligand of oxalic acid, Opt Mater. 88 (2019) 385–391, https://doi.org/10.1016/j.optmat.2018.11.046.
[49] M. Sheikh-Bahae, A.A. Said, T.-H. Wei, D.J. Hagan, E.W. Van Stryland, Sensitive measurement of optical nonlinearities using a single beam, IEEE J. Quant. Electron. 26 (1990) 760–769, https://doi.org/10.1109/3.53394.
[50] M. Mohanraj, T.C. Sabari Girisun, M. Parthasarathy, Growth and multifaceted characterisation of phosphonium-based NLO single crystal: an efficient material for device and optical limiting applications, Opt. Mater. 169 (2026) 117693, https://doi.org/10.1016/j.optmat.2025.117693.
[51] S.R. Meeraa, M. Parthasarathy, Synthesis and characterisation of single crystals of creatininium hydrochloride for third-order NLO applications, Cryst. Res. Technol. 59 (2024) 2300133, https://doi.org/10.1002/crat.202300133.